ERF
European Rotorcraft Forum

EXPERIMENTAL WIND-TUNNEL TESTING OF ROTOR/WAKE AERODYNAMIC INTERACTIONS ON A COMPOUND HELICOPTER

Andrea Colli, Politecnico di Milano, Milano, Italy
Alex Zanotti, Politecnico di Milano, Milano, Italy
Giuseppe Gibertini, Politecnico di Milano, Milano, Italy

Abstract

The compound helicopter configuration has gained renewed interest as a low-range, high-speed rotorcraft. Given the proximity of main rotor and propellers, this configuration is characterised by the aerodynamic interaction between these elements. To investigate the extent of these interactions, a wind-tunnel test campaign was carried out on a model rotor equipped with two lateral propellers, and numerous flight conditions were tested, including low-speed forward flight and crosswind, to study the impact on the aerodynamic performances of the rotors. Numerical simulations with a mid-fidelity code were also performed to further examine the interactional behaviour. The results show an important influence of the main rotor on the propellers, causing a general increase in the generated thrust and in the efficiency, directly related to the main rotor's downwash. A singular occurrence of thrust decrease highlights the complexity of the aerodynamic interactions and their dependence on the flight conditions.

1 NOTATION

a	speed of sound $[\mathrm{m/s}]$
c	chord $[\mathrm{m}]$
CFD	computational fluid dynamics
C_nM^2	sectional normal force coefficient, $C_nM^2 = \frac{F_n}{\frac{1}{2}\rho a^2 c}$
$C_{Q,MR}$	main rotor torque coefficient, $C_{Q,MR} = \frac{Q_{MR}}{\pi\rho\Omega^2 R^5}$
$C_{Q,RP}$	propeller torque coefficient, $C_{Q,RP} = \frac{Q_{RP}}{\rho n^2 D^5}$
$C_{T,MR}$	main rotor thrust coefficient, $C_{T,MR} = \frac{T_{MR}}{\pi\rho\Omega_{MR}^2 R_{MR}^4}$
$C_{T,RP}$	propeller thrust coefficient, $C_{T,RP} = \frac{T_{RP}}{\rho n^2 D^4}$
D	propeller diameter $[\mathrm{m}]$
EJ	flexural rigidity $[\mathrm{N\,m^2}]$
EMS	emergency medical services
FM	main rotor figure of merit, $FM = \frac{C_{T,MR}^{3/2}}{\sqrt{2}C_{Q,MR}}$
F_n	normal force $[\mathrm{N}]$
GJ	torsional rigidity $[\mathrm{N\,m^2/rad}]$
LP	left propeller
m	blade mass per unit length $[\mathrm{kg/m}]$
$\mathrm{Ma_{tip}}$	blade tip Mach number
MR	main rotor
n	propeller revolutions per second $n = \frac{\Omega}{2\pi}$ $[1/\mathrm{s}]$
Q	torque $[\mathrm{N\,m}]$
Q_{crit}	Q-criterion
R	radius $[\mathrm{m}]$
r	blade span-wise coordinate $[\mathrm{m}]$
RP	right propeller
SAR	search and rescue
T	thrust $[\mathrm{N}]$
U_{ave}	average of velocity magnitude $[\mathrm{m/s}]$
U_{rms}	root mean square of velocity magnitude $[\mathrm{m/s}]$
V_∞	free-stream speed $[\mathrm{m/s}]$
V_{tip}	blade tip velocity $[\mathrm{m/s}]$
VTOL	vertical take-off and landing
η_{RP}	propeller efficiency, $\eta_{RP} = \frac{C_{T,RP}}{C_{Q,RP}}$
ϑ_0	main rotor collective pitch angle [deg]
μ	advance ratio, $\mu = \frac{V_{\mathrm{tip,\,MR}}}{V_\infty}$
ρ	air density $[\mathrm{kg/m^3}]$
φ	blade azimuth angle [deg]
ψ	angle of free-stream direction [deg]
Ω	rotational speed $[\mathrm{rad/s}]$

Subscripts:

LP	left propeller
MR	main rotor
RP	right propeller

2 INTRODUCTION

In the quest for vertical flight, the compound helicopter is certainly not a newcomer, as the first examples of this design appeared around the middle of the last century. In broad terms, a compound helicopter features a main rotor with the addition of one or more propellers, and/or supplemental lifting surfaces, acting as wings. The main purpose of this augmentation is to tackle the principal limitation of the traditional helicopter, namely the relatively low maximum speed attainable in forward flight. The well-known reasons for this shortcoming are purely aerodynamic in kind, and related to the composition of the air velocity due to forward motion and the velocity due to the rotational motion, as seen by the blades. On the advancing side of the rotor, the critical Mach number is soon reached, with the ensuing compressibility effects limiting the generation of lift by the blade; on the retreating side, the low resultant speed imposes a high pitching angle for the blade, and the insur-

gence of stall similarly restrict the obtainable lift. This speed limitation of conventional helicopters is particularly unfortunate, as many applications requiring Vertical Take-off and Landing (VTOL) capabilities, for example Emergency Medical Services (EMS) and Search and Rescue (SAR) operations, would greatly benefit from increased cruise velocities.

The idea behind the compound helicopter is to unload the main rotor, relieving it of a portion of the thrust (through the propellers) and lift (through the wings) forces necessary for the forward flight, so that lower rotational speeds as well as lower pitch angles can be employed, effectively postponing the aforementioned aerodynamic limits to higher flight speeds and extending the flight envelope. As mentioned above, the research on compound helicopters begun in the 1950s, but, despite successful aircraft such as the Fairey Rotodyne and the Lockheed AH-56 Cheyenne, the concept was soon essentially abandoned in favour of tilt-rotor and tilt-wing configurations [1, 2]. In recent years, however, there as been a resurgence in the interest in compound rotorcraft [3, 4, 5, 6], as a mobility gap for short-range transport has been identified, which could be efficiently filled by this design; among the aircraft recently developed are the Piasecki X-49, the Eurocopter X^3, the Sikorsky–Boeing SB-1 Defiant, and the Airbus RACER.

Naturally, the presence of the additional components result in an increased complexity of the whole aircraft, which provides new challenges in the design and operating phases. From the point of view of aerodynamics, in particular, one of the main points of interest is represented by the interactions between the main rotor, propellers, and wings, especially considering their wakes, and the effect they have on the aerodynamic performances, vibratory loads, and noise production. Because of the hiatus in the research on compound configurations, the available literature on this topic is scarce, and mainly features computational fluid dynamics (CFD) studies: a comprehensive investigation of a complete compound aircraft, composed of a main rotor, two lateral propellers, and wings is reported in [7, 8, 9, 10, 11], considering various flight conditions; hovering flight CFD simulations of a configuration with main rotor and twin propellers are presented also in [12, 13]. Recently, in the framework of the GARTEUR Programme, the Action Group AG-25 was specifically focused on rotor-rotor and rotor-wake interactions [14]; among the activities involved in this collaboration, which also include the present work, the research by [15] provides an experimental study of the aerodynamic interactions of a main rotor and a single lateral propeller in different advanced flight regimes, followed by a computational study of the same tests. It is interesting to notice that the aforementioned studies agrees on the overall effects of the aerodynamic interactions on the rotors' performances, namely reporting an increased propeller thrust induced by the main rotor, while the reciprocal effect of the propeller on main rotor thrust is very small, if any.

The aim of the work described in the present paper was to conduct a wind-tunnel test campaign on a simplified compound helicopter model, to further study from an experimental point of view the effects of rotor-rotor and rotor-wake interactions on the aerodynamic performances. A test rig composed of a main rotor, two lateral propellers and wing stubs was developed, and various flight conditions were tested, including hovering, low-advance ratio forward flight and different wind directions, representing lateral gust or lateral flight. Finally, the mid-fidelity coupled aeroelastic code DUST+MBDyn [16, 17], was used to numerically reproduce the tested conditions and gain a better insight on the involved phenomena.

3 DISCUSSION

3.1 Test campaign

The tests were performed in the Large Wind Tunnel at Politecnico di Milano, a closed-circuit system with a maximum speed of $55\,\mathrm{m/s}$ and a test section of $4\,\mathrm{m}$ by $3.84\,\mathrm{m}$, which was configured with the open-jet layout for the campaign (Figure 1).

Figure 1: Test rig setup in the wind tunnel; the flow is from left to right in the image.

The chosen compound helicopter configuration features a main rotor and two lateral pusher propellers. The wind-tunnel test rig (Figure 2) was composed of a five-bladed, fully-articulated rotor head mounted on a whirl tower assembly, courtesy of Leonardo Helicopters. The tower's pylon can be rotated and tilted, to achieve different rotor attitudes in terms of mast inclination and yaw angle, or, equivalently, wind direction. The rotor is driven by an electrical motor with a maximum power of $160\,\mathrm{kW}$ and a maximum torque of $500\,\mathrm{N\,m}$. A custom six-component, strain-gage balance is housed in the pylon, measuring the loads acting on the rotor; in particular, a maximum static thrust of $3200\,\mathrm{N}$ is admissible, with a maximum error of $0.4\,\%$. A separate sensor measured the rotor's torque, while Hall-effect magnetic sensors installed in correspondence with the blades' hinges allow the acquisition of the pitch, flap and lag angles. Relatively simple rectangular, untwisted blades were employed,

made of carbon fibre, with NACA 0012 airfoil section and a chord of $0.06\,\mathrm{m}$, for a total rotor radius of $0.858\,\mathrm{m}$. The main rotor was operated at 2200 RPM, corresponding to a tip Mach number of around $\mathrm{Ma}_{\mathrm{tip}} = 0.58$. The main rotor characteristics are summarised in Table 1.

Radius	R_{MR}	$0.858\,\mathrm{m}$
Chord	c_{MR}	$0.06\,\mathrm{m}$
Root cut-out	-	$0.256\,\mathrm{m}$
Airfoil	-	NACA 0012
Rotational speed	Ω_{MR}	2200 RPM

Table 1: Main rotor characteristics.

The five-bladed propellers were based on off-the-shelf hub and blades from VarioProp, for a propeller diameter of $0.3\,\mathrm{m}$. Both right- and left-handed blades are available, and the pitch of the blades can be manually adjusted. More details about the blades, including chord and twist distribution and aerodynamic sections, are available in [18, 19]. A $5.3\,\mathrm{kW}$ Scorpion brushless electrical motor powered each propeller, and bi-axial Futek load cells were employed to measure thrust and torque, up to a maximum of $223\,\mathrm{N}$ and $5.7\,\mathrm{N\,m}$, respectively, with a non-linearity of $\pm 0.25\,\%$ RO. The motor and load cell were housed in a nacelle cowling and the propellers' assemblies were mounted on a steel structure, attached to the rotor pylon. The propellers' centres were positioned $0.285\,\mathrm{m}$ below the main rotor's disk, and $0.362\,\mathrm{m}$ behind and $0.525\,\mathrm{m}$ on either side of the pylon axis; a picture of the assembly is shown in Figure 2. Fairings were added to the support structure, using a NACA 0018 airfoil shape; while the presence of the fairings could be taken to represent wings, as common in this kind of compound configuration, no specific measurement was acquired on them, nor their influence was explicitly studied, the focus being on the interaction between the rotors. As already mentioned, the propellers were mounted in a pusher configuration, but, given the low advance ratios involved, it was deemed more realistic to have the propellers achieving an anti-torque effect with respect to the main rotor; the left propeller, therefore, was set to generate reverse thrust. Both propellers spun at a nominal speed of 8300 RPM in an inboard-up direction; no synchronisation between the main rotor and the propellers was sought.

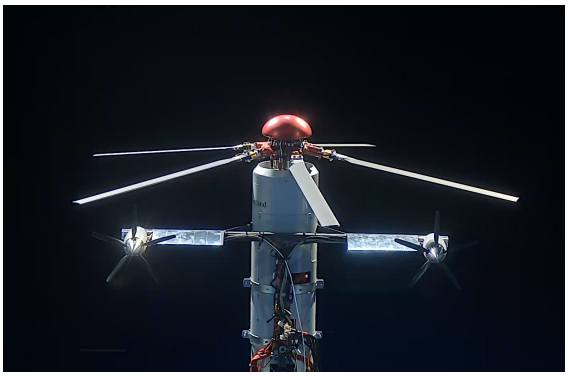

Figure 2: Close-up of the upper portion of the test rig, including the main rotor and the lateral propellers; view from behind.

Different flight conditions were tested, in terms of wind speed and direction, corresponding to hovering, forward flight, and crosswind conditions. Only low advance ratios were considered, as the rotor-wake interactions are less prominent for higher flight speed, as the wakes are convected away from the aircraft. The different test conditions were realized by varying the wind-tunnel speed V_∞ and adjusting the yaw of the rotor pylon, resulting in an equivalent wind direction ψ: a summary of these conditions is reported in Table 2, where μ is the advance ratio $\mu = V_\infty / \Omega R$, with Ω and R being the main rotor rotational speed and radius, respectively.

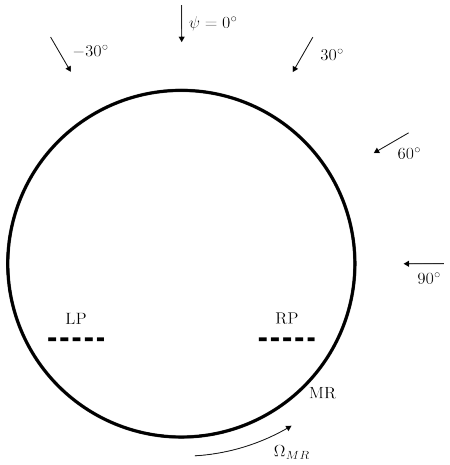

Figure 3: Schematics of the test rig, view from above; the main rotor (MR), right propeller (RP) and left propeller (LP) are indicated, as well as the wind directions ψ considered in the tests.

μ	ψ
0	$0°$
0.025	$-30°$, $0°$, $30°$, $60°$, $90°$
0.05	$-30°$, $0°$, $30°$, $60°$, $90°$
0.1	$0°$

Table 2: Summary of test conditions as a combination of advance ratio μ and wind direction ψ.

To determine the installation effects, that is, the variations due to the interactions between main rotor and propellers, each test was performed with only the main rotor active (MR), with only the propellers active (RP+LP), and with both propellers and main rotor active (MR+RP+LP). Moreover, conditions considering only the main rotor and the right propeller were also tested (RP and MR+RP), in order to investigate the interactions between the two lateral propellers; in this latter configuration, the influence of the propeller's rotational speed was studied by performing a series of test with a propeller's rotational velocity of 9300 RPM. Further information on the influence of other variables, e.g. the direction of rotation, can be found in [20].

Ahead of the main test phase, the main rotor behaviour was characterised by measurements in hovering flight at different collective pitch angles ϑ_0. The interaction tests were conducted by fixing $\vartheta_0 = 7^\circ$ and zero-flapping trim conditions for the cyclic pitch; for the case with $\mu = 0.1$, the collective pitch was lowered to $\vartheta_0 = 6^\circ$ to keep the thrust value similar to the other cases. Finally, the propellers' pitch was adjusted to achieve a nominal value of 23° at the section placed at the $75\,\%$ of the radius, although after the manual adjustment the pitch value of the left propeller was measured to be 22°.

3.2 Experimental results

The interactional effects were evaluated by considering the thrust C_T and torque C_Q coefficients of main rotor and propellers, defined as follows: for the main rotor,

$$(1) \quad C_{T,MR} = \frac{T_{MR}}{\pi\rho\Omega_{MR}^2 R_{MR}^4} \quad \text{and} \quad C_{Q,MR} = \frac{Q_{MR}}{\pi\rho\Omega^2 R_{MR}^5},$$

and for the propellers,

$$(2) \qquad C_{T,RP} = \frac{T_{RP}}{\rho n^2 D_{RP}^4} \quad \text{and} \quad C_{Q,RP} = \frac{Q_{RP}}{\rho n^2 D_{RP}^5};$$

in the formulae above, T is the generated thrust, Q the required torque, Ω the rotational speed, n the number of revolutions per second, R the rotor radius, D the propeller diameter, ρ the air density, and the subscript specifies the component to which the quantity is referred.

From the two coefficients, an indication of the efficiency is obtained by computing the figure of merit FM for the main rotor and a simplified efficiency η for the propellers, given by

$$(3) \qquad FM = \frac{C_{T,MR}^{3/2}}{\sqrt{2} C_{Q,MR}} \quad \text{and} \quad \eta_{RP} = \frac{C_{T,RP}}{C_{Q,RP}},$$

respectively.

Finally, for the main rotor and propellers the sectional normal force coefficient $C_n M^2$ was defined as

$$(4) \qquad C_n M^2 = \frac{F_n}{\frac{1}{2}\rho a^2 c},$$

where F_n is the normal force, a the speed of sound and c the local blade chord.

3.2.1 Main rotor

The experimental results concerning the installation effects on main rotor thrust coefficient C_T are shown, as a function of the yaw angle ψ, in Figure 4 and 5 for the two advance ratios $\mu = 0.025$ and $\mu = 0.05$, respectively, while Figure 6 shows the results for forward flight ($\psi = 0^\circ$) at different advance ratios. It can be seen that for $\mu = 0.025$ the installation effects amount to an increase in the thrust of about $2.8\,\%$ for $\psi = 30^\circ$ and $5.6\,\%$ for $\psi = 90^\circ$, while the increase is almost negligible for the other two wind directions. The effect is reduced for $\mu = 0.05$, where the highest increase is of about $1.5\,\%$. A negative installation effect is recorded for purely forward flight at high advance ratio, as shown also in Figure 6. These results are comparable to the findings reported in literature, where they have been related to a blockage effect of the propellers' wakes on the main rotor inflow [15].

The dependence on the wind direction and speed could be explained by the fact that, for lateral wind and low advance ratio, the propellers' wakes remain closer and directly below the main rotor's disk in a larger region, especially for what concerns the right propeller. The torque of the main rotor is found to slightly increase for all test cases, leading to the trend in the installation effect on the figure of merit shown in Figure 7, where ΔFM represents the variation in the figure of merit between the complete configuration and the main rotor, emphasising the positive influence of the wind direction.

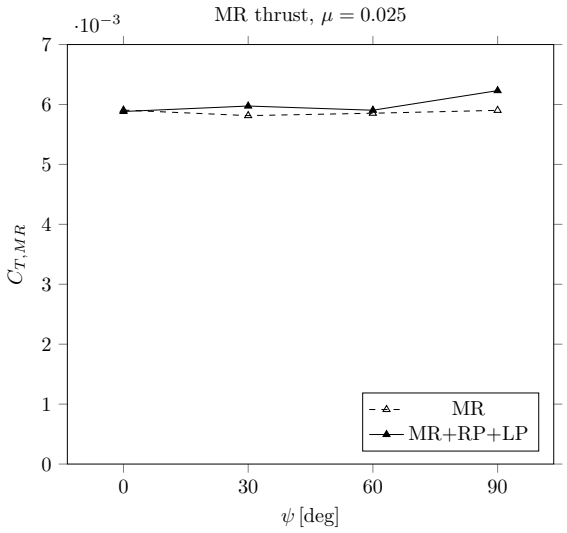

Figure 4: Main rotor's thrust as a function of wind direction for $\mu = 0.025$, comparison between the isolated main rotor (MR) and the complete configuration (MR+RP+LP).

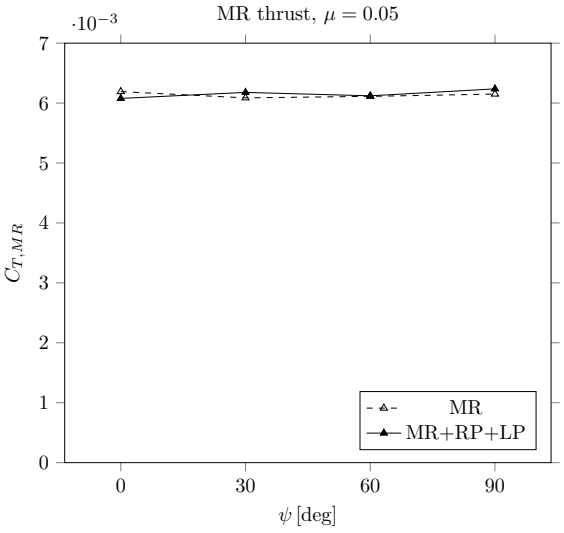

Figure 5: Main rotor's thrust as a function of wind direction for $\mu = 0.05$, comparison between the isolated main rotor (MR) and the complete configuration (MR+RP+LP).

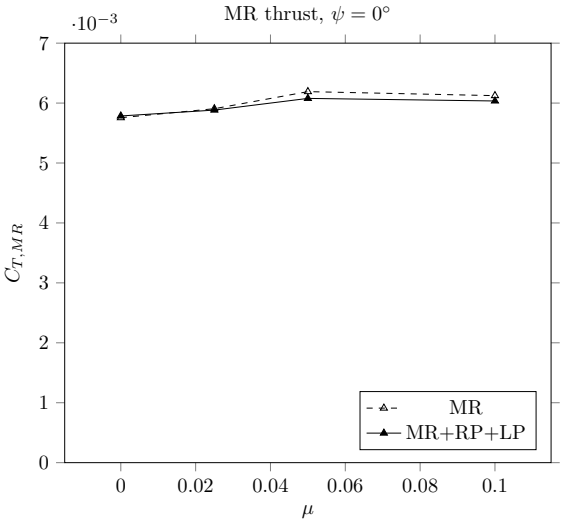

Figure 6: Main rotor's thrust as a function of advance ratio for $\psi = 0°$, comparison between the isolated main rotor (MR) and the complete configuration (MR+RP+LP).

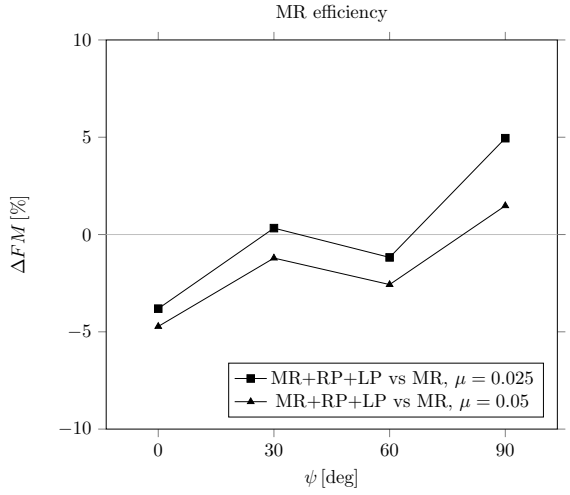

Figure 7: Installation effect on the main rotor's figure of merit for crosswind conditions.

3.2.2 Right propeller

The effects of the presence of the main rotor on the propellers are more noticeable. For the right propeller, as can be seen in Figure 8, a consistent thrust increase above $8\,\%$ is recorded for $\mu = 0.025$, reaching a maximum of $15\,\%$ for $\psi = 90°$. The increase is similar for the conditions with $\mu = 0.05$, up to a maximum of $17\,\%$ (Figure 9), although an immediately noticeable exception is represented by the condition $\mu = 0.05, \psi = 30°$, for which the thrust decreases by $1\,\%$ with respect to the case with the isolated propellers. A positive effect is observed also for forward flight, except at the highest advance ratio (Figure 10), and in general, an increase in the propeller's efficiency was measured, as seen in Figure 11, which reports the difference in efficiency $\Delta\eta$ between the complete configuration and the isolated propellers case.

The increase in thrust can be explained by considering that, for all the conditions tested, the propeller is, at least partially, immersed in the main rotor's downwash, which has two main effects. Firstly, it induces an edgewise velocity component on the propeller's disk: this downward tangential component acts to increase the velocity seen by the upstroking blade, i.e. on the inboard side, and to decrease the velocity seen by the downstroking blade; the propeller load distribution is thus characterised by a lateral asymmetry, which also produces an out-of-plane moment. Secondly, the main rotor's downwash displaces the propeller's wake downward, therefore tending to reduce its induced inflow on the upper part of the propeller's disk, while increasing it in the lower region. These conditions in which the propeller operates are analogous to those experienced by a helicopter rotor in forward flight, and result in a net increase in the thrust generated by the propeller, as had already been known for some time [21, 22, 23]. The main difference with respect to a rotor in forward motion is that the downwash insisting on the propeller is not uniform, but varies radially depending on the load distribution of the main rotor above.

Moreover, the fact that the thrust increase due to the interaction is shown to be greater for the higher values of ψ, and of μ, is consistent with the fact that, in these cases, the main rotor's wake is mainly convected leftward, so that the up-stroking region of the right propeller's disk is favourably affected by the downwash, while the down-stroking portion is partially outside the downwash area, which would decrease its thrust.

Another fundamental difference with a rotor in forward flight is that the main rotor's wake is characterised by the presence of vortical structures, particularly of the tip vortices. The peculiar drop in the generated thrust observed for $\mu = 0.05, \psi = 30^\circ$ could be explained as a blade-vortex interaction (BVI) event, which have been shown to influence the performance of the blade and also trigger flow separation [24, 25, 26, 27]. This hypothesis needs further investigation, but it would explain the occurrence only for these specific wind conditions, as BVI is a local event and in other conditions the tip vortices would not interact with the propeller's blade, or would interact differently and not induce any deterioration of the performances.

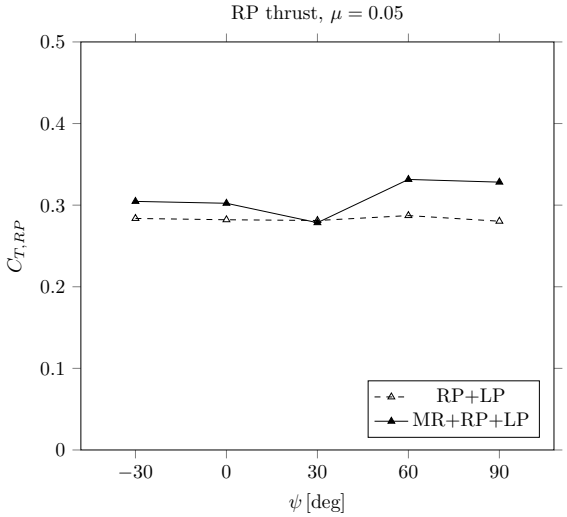

Figure 9: Right propeller's thrust as a function of wind direction for $\mu = 0.05$, comparison between the isolated propellers (RP+LP) and the complete configuration (MR+RP+LP).

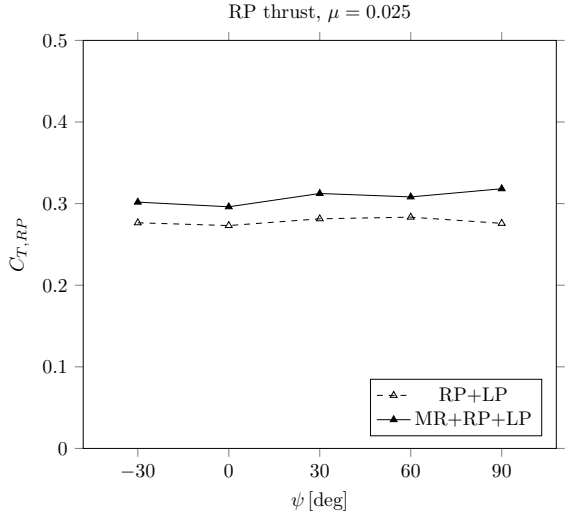

Figure 8: Right propeller's thrust as a function of wind direction for $\mu = 0.025$, comparison between the isolated propellers (RP+LP) and the complete configuration (MR+RP+LP).

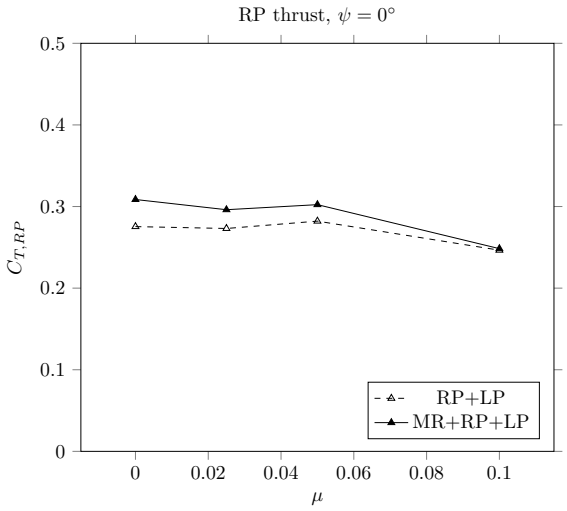

Figure 10: Right propeller's thrust as a function of advance ratio for $\psi = 0^\circ$, comparison between the isolated propellers (RP+LP) and the complete configuration (MR+RP+LP).

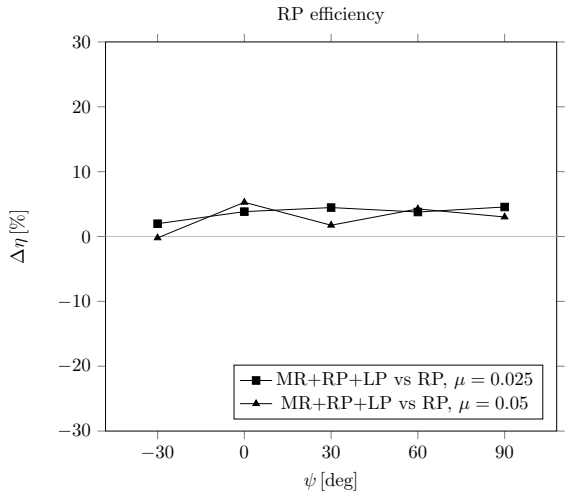

Figure 11: Installation effect on the right propeller's efficiency for crosswind conditions.

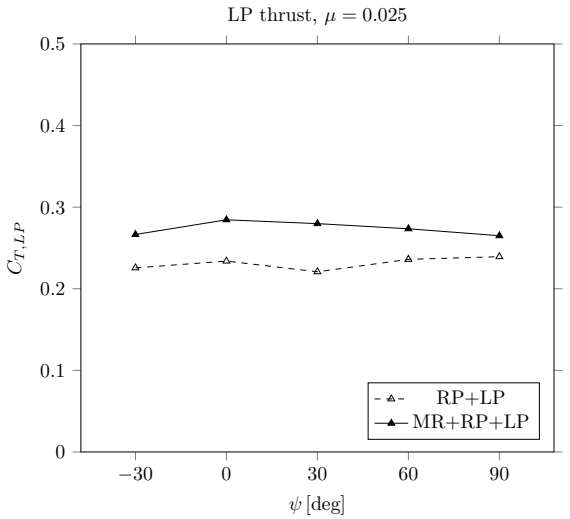

Figure 12: Left propeller's thrust as a function of wind direction for $\mu = 0.025$, comparison between the isolated propellers (RP+LP) and the complete configuration (MR+RP+LP).

3.2.3 Left propeller

Similar considerations to the above ones can be also applied to the analysis of the left propeller thrust values, seen in Figures 12, 13, and 14: the general increase is even greater than for the right propeller, up to $26.7\,\%$ for $\mu = 0.025$ and $35.4\,\%$ for $\mu = 0.05$. This larger effect could be expected since the left propeller is essentially operating in reverse thrust conditions, forcing its wake to stay closer to the propeller itself, in a vortex ring state; the convection of the wake by the main rotor downwash, therefore, would have a beneficial effect on the propeller performances. Correspondingly, a large increment of the propeller's efficiency is measured for all cases Figure 15. In applying the reasoning about the main rotor's downwash influence from the previous section, however, it should be taken into account the fact that for the higher values of ψ the left propeller could be partially shadowed by the other parts of the test rig, particularly the pylon.

Interestingly, no particular condition for which the propeller thrust decreases, or does not increase as much, can be observed. This fact supports the interpretation given above about the interaction of the right propeller with the main rotor tip vortices, which would not happen to the left propeller given its upwind position with respect to the main rotor blade tips for the wind directions tested, except for $\psi = -30°$.

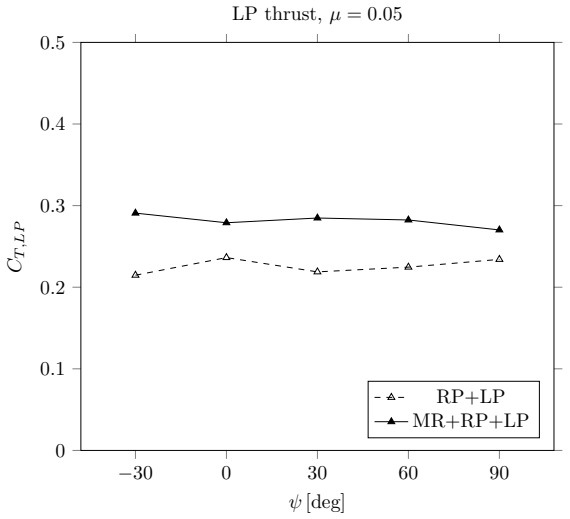

Figure 13: Left propeller's thrust as a function of wind direction for $\mu = 0.05$, comparison between the isolated propellers (RP+LP) and the complete configuration (MR+RP+LP).

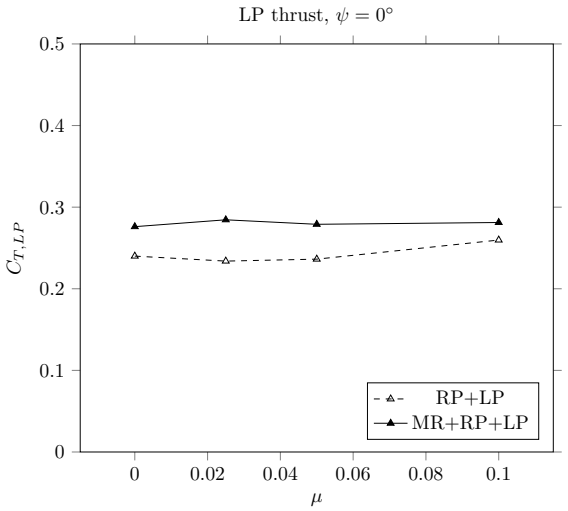

Figure 14: Left propeller's thrust as a function of advance ratio for $\psi = 0°$, comparison between the isolated propellers (RP+LP) and the complete configuration (MR+RP+LP).

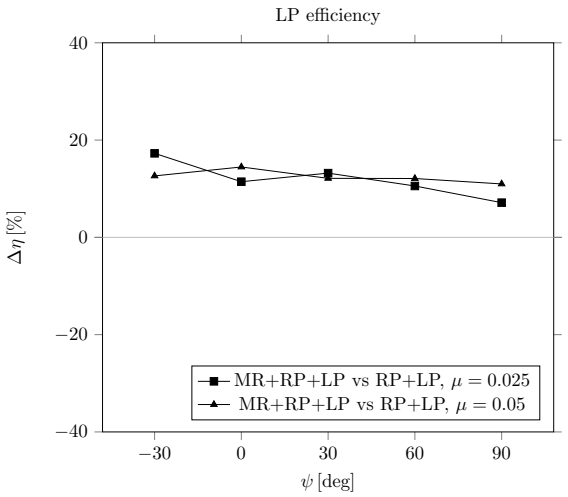

Figure 15: Installation effect on the left propeller's efficiency for crosswind conditions.

3.2.4 Right propeller only

Concerning the tests with only the main rotor and the right propeller, Figure 16 shows the effects of the interaction on the thrust of the right propeller, for $\mu = 0.05$: by comparing to Figure 9, it can be seen how the trend is similar, with a general increase in thrust, and also featuring the drop below the isolated value for $\psi = 30°$. The lower increase measured for $\psi = 0°$, compared to the configuration with both right and left propeller, could hint at an influence of the left propeller, which is reduced at the higher ψ as its wake is convected away from the right propeller by the free-stream flow.

Finally, Figure 17 compares the thrust generated by the right propeller during the interaction with the main rotor, considering two different rotational speeds, showing that no significant difference in the behaviour can be observed between these cases.

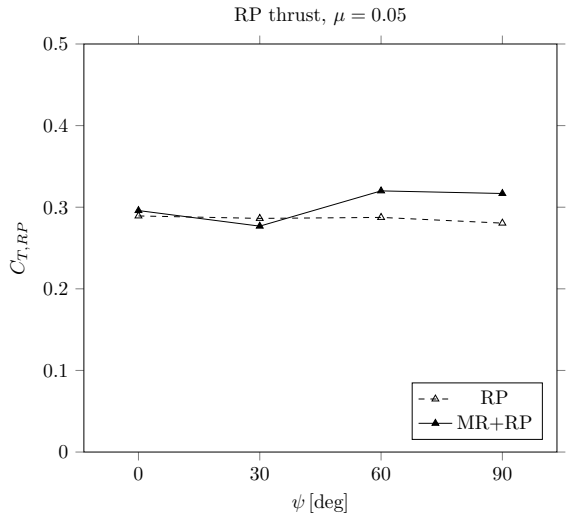

Figure 16: Right propeller's thrust as a function of wind direction for $\mu = 0.05$, comparison between the isolated right propeller (RP) and the configuration with main rotor and right propeller active (MR+RP).

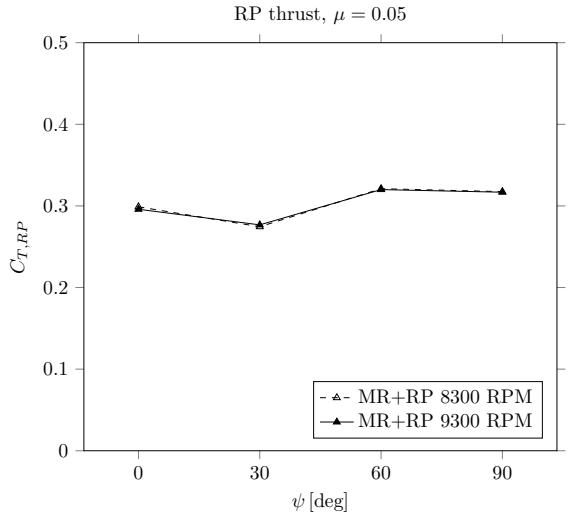

Figure 17: Right propeller's thrust as a function of wind direction for $\mu = 0.05$, comparison between the configurations with main rotor and right propeller spinning at different speeds.

3.3 Numerical simulations

Given the complexity of the test configuration, featuring three five-bladed rotors spinning at very different speeds, and the large number of conditions to be considered, the mid-fidelity vortex-particle aerodynamic code DUST was chosen for the numerical simulations, given its ability to easily model multiple rotors and their wakes, describing interactional aerodynamics at a relatively low time cost.

3.3.1 Numerical model

As a first modelisation of the test rig, main rotor and propeller were described using lifting line elements, with a spanwise discretization of 20 and 30 panels, respectively. Aerodynamic data for the propeller's blade sections were computed employing XFOIL [28]. The propellers' nacelles were included, but the fairings and the rotor pylon were excluded.

Firstly, to validate the model, the main rotor alone in hovering flight was simulated and compared to experimental measurements from the test campaign; the results, reported in Figure 18, show an agreement between DUST and the experimental data only for the lowest collective pitch angles, while an underestimation of the thrust is evident at the higher collectives.

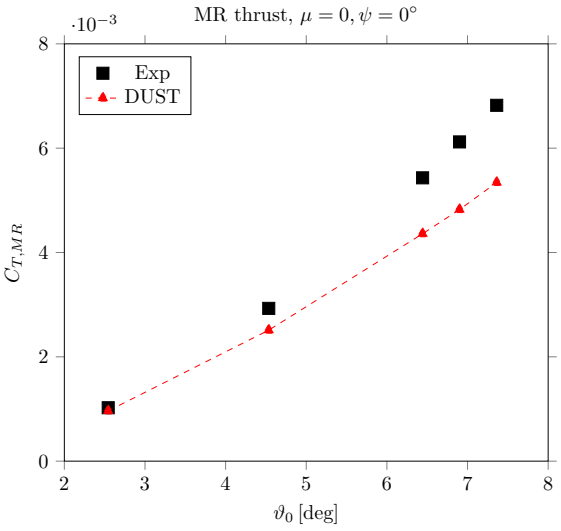

Figure 18: Main rotor's thrust coefficient variation with collective pitch angle ϑ_0 in hovering flight, comparison between the experimental measurements and the results from DUST simulations.

Given the worsening of the discrepancy at the higher collective pitch angles, and thus with the higher rotor loads, the effect was attributed to a torsional deformation of the blades. In order to evaluate this hypothesis, static tests, both non-destructive and destructive, were performed on the blades to measure the relevant structural quantities, in particular the torsional rigidity and the chordwise position of the elastic axis and the centre of mass of the blade sections; the results are reported in Table 3, and show a plausible increase of the blade incidence due to torsion, given the position of the elastic axis behind the aerodynamic centre.

In order to include in the simulations the torsional and bending behaviours of the blades, the aeroelastic suite featuring the coupling of DUST with MBDyn, a multibody dynamic solver, was employed [17]. The model was updated with the structural data of the blades, and the main rotor description by lifting lines was changed to use non-linear vortex lattice element [29], with a chordwise discretisation of 30 panels, which allows accurately modelling the distribution of the aerodynamic load. The results from this updated model show a remarkably better agreement with the experimental data (Figure 19), indicating that blade torsion could be an effective explanation.

Mass per unit length	m	$0.221\,\mathrm{kg/m}$
Flexural rigidity	EI	$33.2\,\mathrm{N\,m^2}$
Torsional rigidity	GJ	$15.4\,\mathrm{N\,m^2/rad}$
Centre of mass chordwise position	-	$40\,\%\ c_{MR}$
Elastic axis chordwise position	-	$29\,\%\ c_{MR}$

Table 3: Measured structural data of the main rotor's blades.

For numerical stability reasons, however, the coupled simulations showed issues for the forward flight test conditions, which diverged before reaching a suitable time span to investigate the interactional effects. The approach was then chosen to perform purely aerodynamic simulations with DUST, using lifting line elements, but including an equivalent twist distribution of the blades to represent the torsion, which was extrapolated from the aeroelastic simulations by time averaging the torsional distribution of the blade. This would naturally impair the accuracy of the model, also given that the twist distribution is constant in time, instead of the cyclically varying torsional deformation. However, the resulting model was deemed sufficient to investigate the general behaviour of the flow-field and the relevant interactions between the rotors, and to obtain at least a qualitative description of the phenomena involved (Figure 19). Following this reasoning, it was also decided to exclude the left propeller from the numerical model, in order to reduce the computational complexity. This choice was justified by the fact that the chief interest involved the right propeller, given the test conditions and the effects measured in the wind tunnel campaign, and by the observation made above that the qualitative behaviour of the interactions on the right propeller was not influenced by the presence of the left propeller.

With this final choice of model, a total of 32 propeller revolutions, corresponding to 8 main rotor revolutions, were simulated for each test condition, and separate simulations were performed on the isolated components, to allow computing the installation effects. Each simulation took about 2 hours on a workstation-level computer.

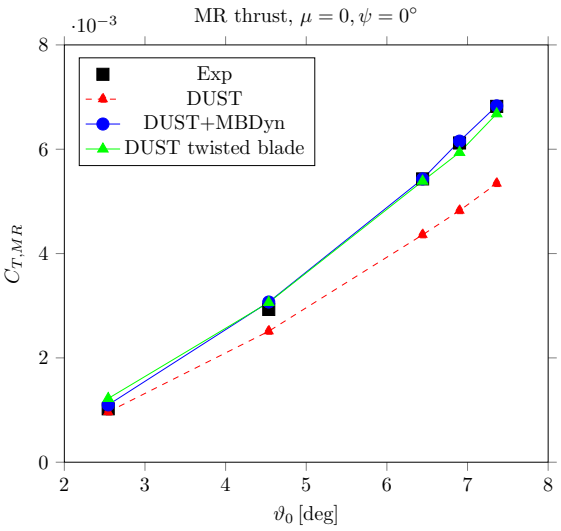

Figure 19: Main rotor's thrust coefficient variation with collective pitch angle ϑ_0 in hovering flight, comparison between the experimental measurements, the results from DUST simulations, DUST+MBDyn aeroelastic simulations and DUST simulations considering an equivalent twist distribution for the blades.

3.3.2 Numerical results

The results of simulations on the test conditions with lateral wind are reported in Figure 20 for what concerns the right propeller thrust. Despite an underestimation of the loads, which can also be attributed to the wings not being modelled, the increase in thrust with respect to the isolated propeller is well-captured, except for the singular thrust loss noticed in the experimental measurements.

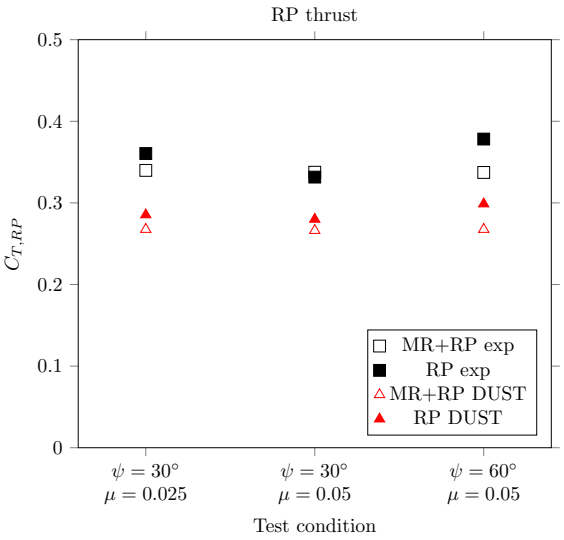

Figure 20: Installation effects on the right propeller's thrust for some test conditions, considering the isolated right propeller (RP) and the configuration with main rotor and right propeller active (MR+RP); comparison between the experimental data and results from the DUST simulations.

To examine more in detail the mechanism producing this increase, the load distribution over the propeller's disk is reported in Figure 21, which shows the difference in sectional normal force coefficient between the case with main rotor and propeller active and the case with only the propeller active, for the condition $\mu = 0.025, \psi = 30°$: the asymmetry in the load distribution is clearly visible, with the left side, corresponding to the upstroking blade, presenting an increase in load, while the right side, the downstroking blade, produces a decrease in the loading with respect to the isolated propeller. This is in accordance with the analysis reported above of the effects of the main rotor's downwash. The load distribution for $\mu = 0.05, \psi = 90°$ is visible in Figure 22, where it is evident that only a smaller portion of the downstroking side of the propeller contributes negatively to the thrust increase due to the interaction. As mentioned above, this effect is attributed to the behaviour of the main rotor's wake as it is convected by the free-stream flow, impacting on different portions of the propeller's disk. This is more clearly visible comparing the load distributions presented above with Figures 23 and 24, which show contours of the average velocity field in the proximity of the propeller, on a plane parallel to the propeller's disk and $0.03\,\mathrm{m}$ in front of it. The edge of the rotor's wake can be seen to pass just over the right edge of the propeller in Figure 23, corresponding to a condition in which the whole propeller is immersed in the main rotor's downwash, while in Figure 24 the rotor's wake, being more strongly convected to the left, insists on only about half of the propeller's disk, the upstroking region.

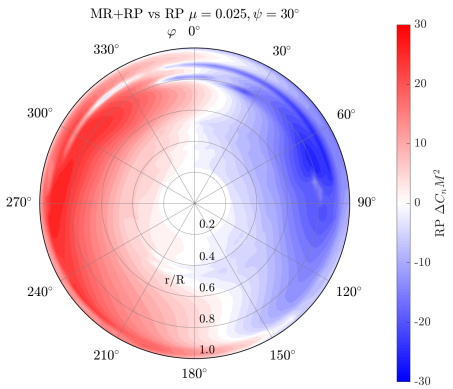

Figure 21: Difference in the sectional load distribution on the right propeller's disk between the configuration with main rotor and right propeller active and the isolated right propeller, for the condition $\mu = 0.025$ and $\psi = 30°$. Results averaged over six propeller revolutions. The azimuth $\varphi = 0°$ corresponds to the blade on top. (Reproduced with permission from [20])

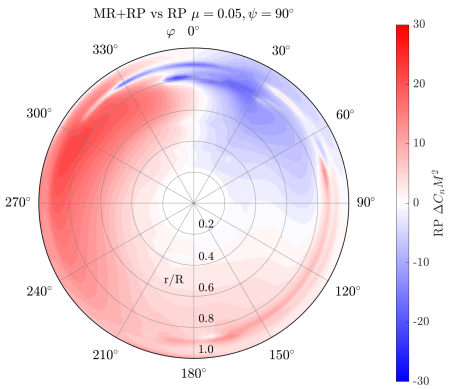

Figure 22: Difference in the sectional load distribution on the right propeller's disk between the configuration with main rotor and right propeller active and the isolated right propeller, for the condition $\mu = 0.05$ and $\psi = 90°$. Results averaged over six propeller revolutions. The azimuth $\varphi = 0°$ corresponds to the blade on top. (Reproduced with permission from [20])

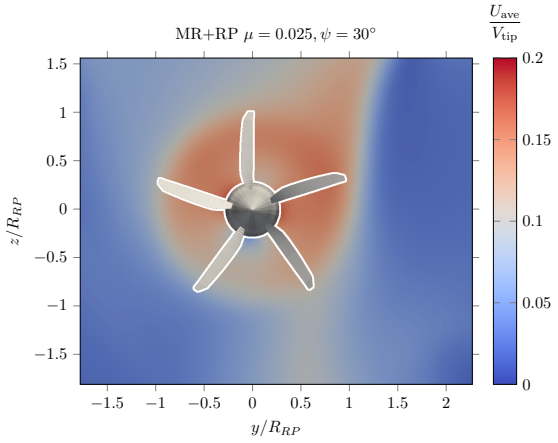

Figure 23: Contours of the velocity magnitude averaged over six propeller's revolutions, for the configuration with main rotor and right propeller active with $\mu = 0.025$ and $\psi = 30°$; view from behind.

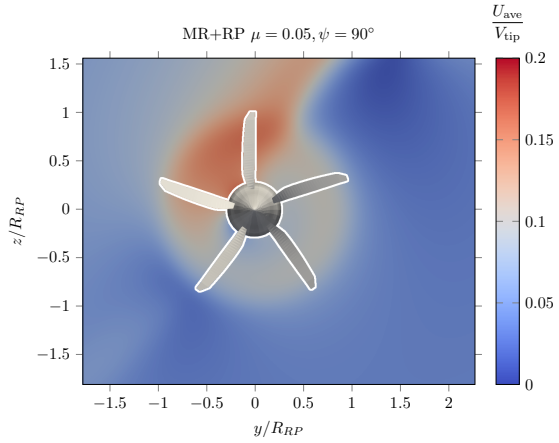

Figure 24: Contours of the velocity magnitude averaged over six propeller's revolutions, for the configuration with main rotor and right propeller active with $\mu = 0.05$ and $\psi = 90°$; view from behind.

The peculiar drop in thrust measured for $\mu = 0.05, \psi = 30°$ was not reproduced by the numerical simulation. This could be attributed to the difficulty of the mid-fidelity method in describing complex local phenomena in which viscosity effects and boundary layer behaviour play a fundamental role. Better insight, however, can be gained by comparing the contours of Q-criterion, identifying the main vortical structures, in the region close to the propeller's disk, as shown in Figure 25. The tip vortices released by the main rotor blades are clearly visible, and their trajectories reveal qualitatively different patterns, depending on wind speed and direction. In particular, for $\psi = 30°$ and $\mu = 0.025$, it can be seen how the tip vortices are convected inboard and intersect the propeller's disk only marginally at its rightmost edge. As they pass near the tip of the clockwise-rotating propeller's blades, they are not directly cut through, but they experience an upward displacement, which produces vortex pairing and results in the formation of clusters of vortical structures. A similar pattern, but more complex, is visible for the case $\psi = 30°$ and $\mu = 0.05$, shown in Figure 26: this behaviour could support the hypothesis of the thrust loss occurring in these condition being determined by a BVI effect. In contrast, for $\psi = 90°$ and $\mu = 0.5$, as shown in Figure 27, the main rotor tip vortices are more strongly displaced inboard, and they intersect the propeller's disk almost diametrically, being disrupted by the passing blades and the nacelle, as can be seen by their reduced intensity. It is to be noticed that the contours described above represent only instantaneous snapshots of the interaction, and that a complete description should also take into account the whole three-dimensional description of the vortical structures.

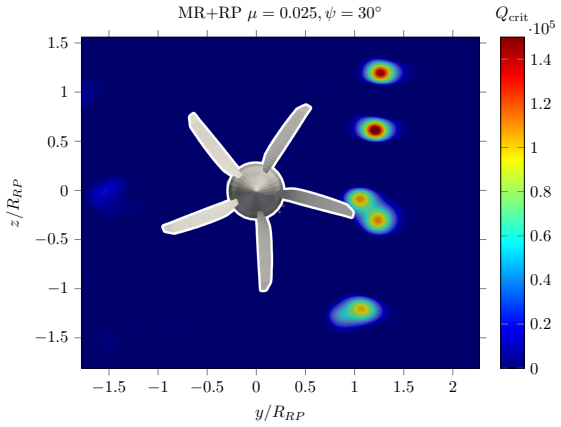

Figure 25: Contours of Q-criterion for the configuration with main rotor and right propeller active with $\mu = 0.025$ and $\psi = 30°$; view from behind.

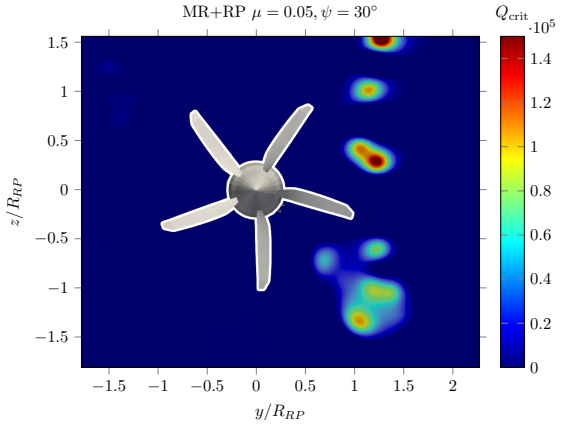

Figure 26: Contours of Q-criterion for the configuration with main rotor and right propeller active with $\mu = 0.05$ and $\psi = 30°$; view from behind.

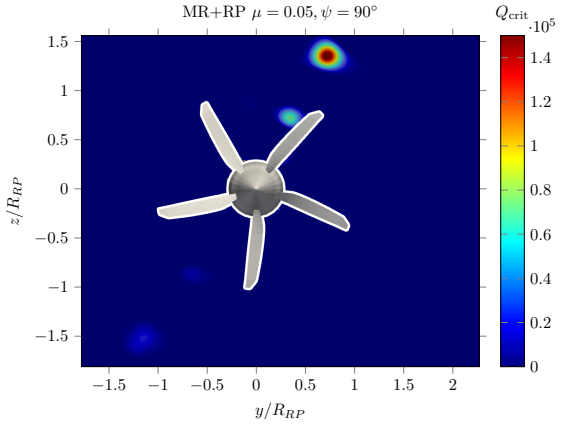

Figure 27: Contours of Q-criterion for the configuration with main rotor and right propeller active with $\mu = 0.05$ and $\psi = 90°$; view from behind.

The different behaviours in the tip vortices trajectories can be evinced also from the contours of the root-mean-square of the velocity, shown in Figures 28, 29, and 30, which identify the region characterised by the permanence of vortical clusters next to the propeller's disk for the three conditions mentioned above.

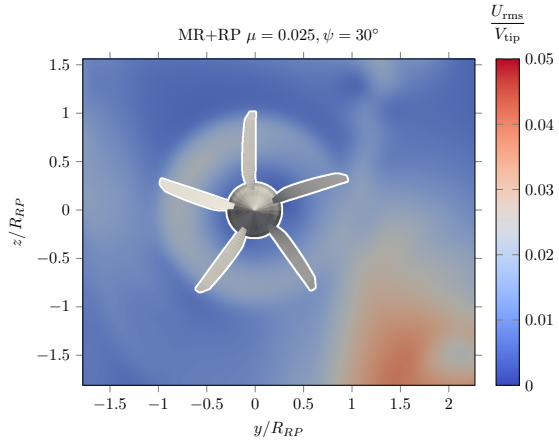

Figure 28: Contours of the root mean square of the velocity magnitude over six propeller's revolutions, for the configuration with main rotor and right propeller active with $\mu = 0.025$ and $\psi = 30°$; view from behind.

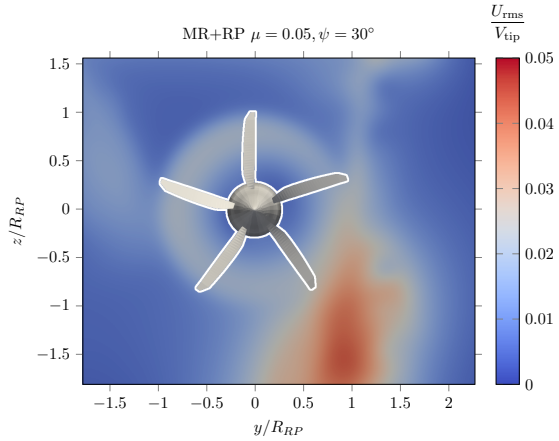

Figure 29: Contours of the root mean square of the velocity magnitude over six propeller's revolutions, for the configuration with main rotor and right propeller active with $\mu = 0.05$ and $\psi = 30°$; view from behind.

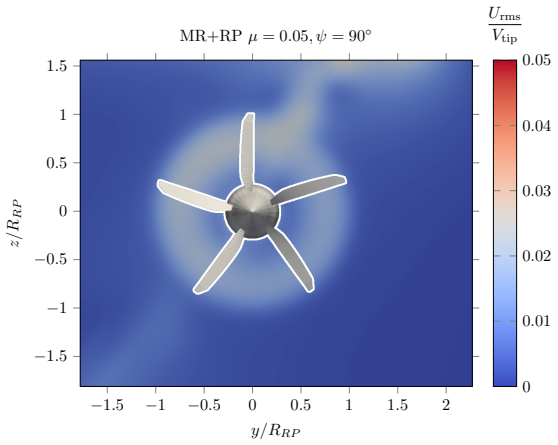

Figure 30: Contours of the root mean square of the velocity magnitude over six propeller's revolutions, for the configuration with main rotor and right propeller active with $\mu = 0.05$ and $\psi = 90°$; view from behind.

Finally, Figure 31 shows the installation effect on the main rotor's load distribution, as the difference in the sectional load coefficient between the configuration with the main rotor and right propeller active and the isolated main rotor: a region of increased loading is visible immediately downwind of the propeller's position, indicating the blockage effect of the propeller's slipstream. Weak variations in the tip portion of the rotor's disk can also be seen, which are probably due to differences in tip vortex interactions, as suggested by [15].

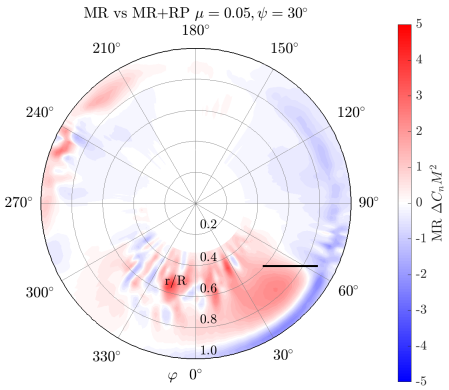

Figure 31: Difference in the sectional load distribution on the main rotor's disk between the configuration with main rotor and right propeller and the isolated main rotor, for the condition $\mu = 0.05$ and $\psi = 30°$. Results averaged over four rotor revolutions. The azimuth $\varphi = 0°$ corresponds to the blade on the rear, and the black segment indicates the position of the propeller's disk.

4 CONCLUSIONS

The present work described the results of a wind-tunnel test campaign on a compound helicopter configuration in different flight conditions, in order to study the effects of the aerodynamic interference between main rotor and lateral propellers. It was found that in general the influence on the main rotor loads is limited, resulting in a slight increase in the generated thrust attributed to the presence of the propellers. On the other hand, the effect of the main rotor's downwash on the propeller is much more marked, with a general increase in the thrust up to $17\,\%$ and $35\,\%$ for the right and left propeller, respectively. These findings are in agreement with the literature on similar configurations, and can be explained by the additional velocity component introduced by the main rotor's downwash impinging on the propellers. For one test condition, however, a negative installation effect, with a decrease in the propeller's thrust, was measured, which was attributed to a local BVI event related to the interaction with the main rotor tip vortices.

The analysis of the experimental results was complemented by mid-fidelity numerical simulations performed with DUST. A relevant torsional effect of the blade was correctly described by the coupled aeroelastic version of the code, while purely aerodynamic simulations, despite not in full agreement with the measured values, correctly captured the effect of the main rotor on the propellers. Moreover, the load distributions extracted from the numerical results and the flowfield descriptions supported the interpretation of the mechanisms of interaction with the main rotor's downwash and tip vortices.

In conclusion, an important increase in the thrust generated by the lateral propeller of a compound helicopter was measured, as a result of the aerodynamic interaction with the main rotor. This effect needs to be accounted for in the design phase of the aircraft, as it can have a relevant impact on the performances and the controllability of the machine. Moreover, the occurrence of an anomalous thrust reduction in some conditions highlights the complexity of the flow and stresses the importance of a complete description of the wake dynamics in response to the flight conditions. To this purpose, a vorticity-based mid-fidelity aerodynamic code proved useful in analysing the interaction mechanisms efficiently, although not all the flow features were captured. Wind-tunnel testing thus maintains a critical role in evaluating the effects of the aerodynamic interactions, as well as high-fidelity CFD. The above considerations are not limited to the configuration examined here, but can be applied to any aircraft in which rotors can be found operating in the slipstream of other rotors.

Author contact:
Andrea Colli andrea.colli@polimi.it
Alex Zanotti alex.zanotti@polimi.it
Giuseppe Gibertini giuseppe.gibertini@polimi.it

Acknowledgements

The authors wish to thankfully acknowledge the support during the experimental campaign by Leonardo Helicopters and by the Aerodynamic Laboratory of the Department of Aerospace Science and Technology at Politecnico di Milano. Moreover, the authors wish to thank the partners of the GARTEUR HC/AG-25.

References

[1] M. N. Orchard and S. J. Newman. The compound helicopter — why have we not succeeded before? *The Aeronautical Journal*, 103(1028):489–495, October 1999.

[2] R. A. Ormiston. Revitalising advanced rotorcraft research – and the compound helicopter. *The Aeronautical Journal*, 120(1223):83–129, January 2016.

[3] DEH Balmford and BS Benger. The compound helicopter: a concept revisited. In *17th European Rotorcraft Forum*, 1991.

[4] M Orchard and S Newman. The fundamental configuration and design of the compound helicopter. *Proceedings of the Institution of Mechanical Engineers, Part G: Journal of Aerospace Engineering*, 217(6):297–315, June 2003.

[5] Martin Blacha, Axel Fink, Paul Eglin, and Philippe Cabrit. Clean Sky 2: Exploring new rotorcraft high speed configurations. In *43rd European Rotorcraft Forum*, 2017.

[6] Marc Wentrup, Jianping Yin, Philipp Kunze, Thomas Streit, Jan-Hendrik Wendisch, Thorsten Schwarz, Jean-Paul Pinacho, Klaus Kicker, and Raphaël Fukari. An overview of DLR compound rotorcraft aerodynamics and aeroacoustics activities within the CleanSky2 NACOR project. In *AHS Forum 2018*, 2018.

[7] Constantin Öhrle, Felix Frey, Jakob Thiemeier, Manuel Keßler, and Ewald Kräamer. Coupled and trimmed aerodynamic and aeroacoustic simulations for Airbus Helicopters' compound helicopter RACER. *Journal of the American Helicopter Society*, 64(3):1–14, July 2019.

[8] Felix Frey, Jakob Thiemeier, Constantin Öhrle, Manuel Keßler, and Ewald Krämer. Aerodynamic interactions on Airbus Helicopters' compound helicopter RACER in cruise flight. In *Proceedings of the Vertical Flight Society 75th Annual Forum*. The Vertical Flight Society, May 2019.

[9] Jakob Thiemeier, Constantin Öhrle, Felix Frey, Manuel Keßler, and Ewald Krämer. Aerodynamics and flight mechanics analysis of airbus helicopters' compound helicopter racer in hover under crosswind conditions. *CEAS Aeronautical Journal*, 11(1):49–66, April 2019.

[10] Felix Frey, Jakob Thiemeier, Constantin Öhrle, Manuel Keßler, and Ewald Krämer. Aerodynamic interactions on Airbus Helicopters' compound helicopter RACER in hover. *Journal of the American Helicopter Society*, 67(1):1–17, January 2022.

[11] Tom Stokkermans, Leo Veldhuis, Bambang Soemarwoto, Raphaël Fukari, and Paul Eglin. Breakdown of aerodynamic interactions for the lateral rotors on a compound helicopter. *Aerospace Science and Technology*, 101:105845, June 2020.

[12] Hideaki Sugawara and Yasutada Tanabe. Numerical investigation of rotor/wing aerodynamic interactions at high advance ratios. *Journal of Aircraft*, 56(6):2285–2298, November 2019.

[13] Keita KIMURA, Hideaki SUGAWARA, and Yasutada TANABE. Aerodynamic interference between main rotor and side propellers of a winged-type compound helicopter in hover. *TRANSACTIONS OF THE JAPAN SOCIETY FOR AERONAUTICAL AND SPACE SCIENCES*, 66(5):174–185, 2023.

[14] Ronan Boisard, Lauriane Lefevre, Tao Zhang, George Barakos, Antonio Visingardi, Felix Lößle, Anna Kostek, Theologos Andronikos, Manuel Keßler, Robin Wickersheim, et al. Rotor/rotor aerodynamic interactions-a Garteur action group. In *ICAS 2022*, pages 3261–3276, 2022.

[15] Ronan Boisard. Numerical analysis of rotor/propeller aerodynamic interactions on a high-speed compound helicopter. *Journal of the American Helicopter Society*, 67(1):1–15, January 2022.

[16] Matteo Tugnoli, Davide Montagnani, Monica Syal, Giovanni Droandi, and Alex Zanotti. Mid-fidelity approach to aerodynamic simulations of unconventional VTOL aircraft configurations. *Aerospace Science and Technology*, 115:106804, August 2021.

[17] Alberto Savino, Alessandro Cocco, Alex Zanotti, Matteo Tugnoli, Pierangelo Masarati, and Vincenzo Muscarello. Coupling mid-fidelity aerodynamics and multibody dynamics for the aeroelastic analysis of rotary-wing vehicles. *Energies*, 14(21):6979, October 2021.

[18] Alex Zanotti. Experimental study of the aerodynamic interaction between side-by-side propellers in eVTOL airplane mode through stereoscopic particle image velocimetry. *Aerospace*, 8(9):239, August 2021.

[19] Alex Zanotti and Davide Algarotti. Aerodynamic interaction between tandem overlapping propellers in eVTOL airplane mode flight condition. *Aerospace Science and Technology*, 124:107518, May 2022.

[20] Andrea Colli, Alex Zanotti, and Giuseppe Gibertini. Wind-tunnel experimental investigation on rotor-rotor aerodynamic interaction in compound helicopter configuration. *Aerospace Science and Technology*, 153:109420, July 2024.

[21] Hiram S Maxim. Screw propellers working in air. *Aeronautical Annual*, 1(3):142–144, 1897.

[22] DP Riabouchinsky. Recherches sur une hélice mise en rotation dans un courant d'air dirigé perpendiculairement à l'axe de l'hélice. *Izvestiya Rossiiskoi Akademii Nauk. Seriya Matematicheskaya*, 24(1):49–52, 1906.

[23] Biel Ortun, Ronan Boisard, and Ignacio Gonzalez-Martino. In-plane airloads of a propeller with inflow angle: Prediction vs. experiment. In *30th AIAA Applied Aerodynamics Conference*. American Institute of Aeronautics and Astronautics, June 2012.

[24] G. Droandi, G. Gibertini, and A. Zanotti. Perpendicular blade–vortex-interaction over an oscillating airfoil in light dynamic stall. *Journal of Fluids and Structures*, 65:472–494, August 2016.

[25] Neal M Chaderjian. Navier-Stokes simulation of UH-60A rotor/wake interaction using adaptive mesh refinement. In *AHS International Annual Forum & Technology Display*, number ARC-E-DAA-TN40776, 2017.

[26] François Richez. Analysis of dynamic stall mechanisms in helicopter rotor environment. *Journal of the American Helicopter Society*, 63(2):1–11, April 2018.

[27] Andrea Colli, Alex Zanotti, and Giuseppe Gibertini. Wind tunnel experiments on parallel blade–vortex interaction with static and oscillating airfoil. *Fluids*, 9(5):111, May 2024.

[28] Mark Drela. Xfoil: An analysis and design system for low reynolds number airfoils. In *Low Reynolds Number Aerodynamics: Proceedings of the Conference Notre Dame, Indiana, USA, 5–7 June 1989*, pages 1–12. Springer, 1989.

[29] Alessandro Cocco, Andrea Colli, Alberto Savino, Pierangelo Masarati, and Alex Zanotti. A non-linear unsteady vortex lattice method for aeroelastic rotor loads evaluation. In *48th European Rotorcraft Forum (ERF 2022)*, pages 1–8, 2022.